Development of a beta spectrometry setup using metallic magnetic calorimeters

M. Paulsen, J. Beyer, L. Bockhorn, C. Enss, S. Kempf, K. Kossert, Martin Loidl, Riham Mariam, O. Nähle, P. Ranitzsch, et al.

Published by IOP Publishing for Sissa Medialab

Received: *May 10, 2019*
Accepted: *July 15, 2019*
Published: *August 8, 2019*

Development of a beta spectrometry setup using metallic magnetic calorimeters

M. Paulsen,[a,b,1] **J. Beyer,**[a] **L. Bockhorn,**[c] **C. Enss,**[b] **S. Kempf,**[b] **K. Kossert,**[c] **M. Loidl,**[d] **R. Mariam,**[d] **O. Nähle,**[c] **P. Ranitzsch**[c] **and M. Rodrigues**[d]

[a] *Physikalisch-Technische Bundesanstalt (PTB), Abbestraße 2-12, 10587 Berlin, Germany*
[b] *Kirchhoff-Institute for Physics (KIP), Im Neuenheimer Feld 227, 69120 Heidelberg, Germany*
[c] *Physikalisch-Technische Bundesanstalt (PTB), Bundesallee 100, 38116 Braunschweig, Germany*
[d] *CEA, LIST, Laboratoire National Henri Becquerel (LNHB), CEA Saclay, 91191 Gif-sur-Yvette Cedex, France*

E-mail: michael.paulsen@ptb.de

Abstract: The precise knowledge of beta spectrum shapes is relevant in radionuclide metrology, e.g. when determining the activity of samples containing beta emitting isotopes, as well as in fundamental research or applications such as nuclear medicine. We present a newly developed beta spectrometer that utilizes Metallic Magnetic Calorimeters (MMCs) which have 4π absorbers and operates at temperatures < 100 mK. Microfabricated MMC detectors designed for five beta energy intervals enable the measurement of beta spectra with endpoint energies E_{max} ranging from a few tens of keV up to ≈ 1 MeV. The different detector types are read out by Superconducting QUantum Interference Device (SQUID) current sensors with compatible input inductances. In particular, we discuss the MMC detector design, absorber/source preparation, data acquisition and handling of the relatively large measurement data sets. The realized setup allows for high resolution beta spectrometry, which was shown via a test measurement of ^{99}Tc ($E_{\mathrm{max}} = 293.8$ keV) using an external photon-emitting ^{241}Am calibration source.

Keywords: Calorimeters; Cryogenic detectors; Data processing methods; Spectrometers

[1] Corresponding author.

https://doi.org/10.1088/1748-0221/14/08/P08012

2019 JINST 14 P08012

Contents

2019 JINST 14 P08012

1 Introduction

Microcalorimeters typically consist of a small absorber that is temperature monitored by a detector. In a Metallic Magnetic Calorimeter (MMC) [1–3] the detector is composed of a metallic paramagnet which is put in a weak magnetic field B and operated at a temperature T_0, as depicted in figure 1. When a particle or radiation deposits the energy ΔE in the absorber, it leads to a temperature increase ΔT. Since the magnetic susceptibility of the paramagnet is strongly temperature dependent, any temperature change will lead to a change in its magnetization M i.e. $\Delta M = (\partial M/\partial T) \cdot \Delta T = (\partial M/\partial T) \cdot (\Delta E/C_{\text{tot}})$, where C_{tot} denotes the total heat capacity of the absorber and the paramagnet. The corresponding magnetic flux change $\Delta\Phi$ can be measured by means of a Superconducting QUantum Interference Device (SQUID) sensor.

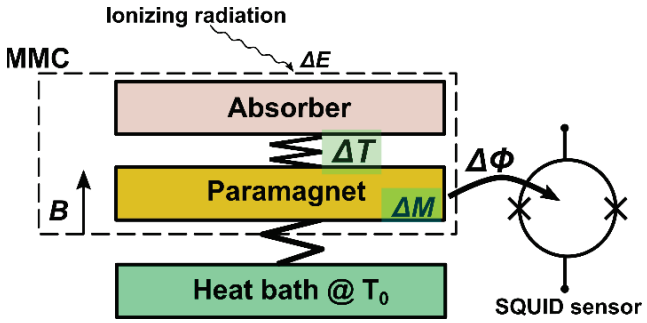

Figure 1. The general working principle of an MMC.

Setups using MMCs with the radionuclide source embedded in a 4π absorber geometry have proven to be among the best beta spectrometers in terms of energy resolution, notably for low-energy beta transitions [4]. The MMC detector of such setups utilizes a magnetically doped noble

metal as a paramagnet, that is put in a weak magnetic field $B \sim 1\,\mathrm{mT}$. The field is produced by two superconducting Nb meandering pickup coils holding a persistent current I, as depicted in figure 2. A persistent field current $\sim 50\,\mathrm{mA}$ is injected to produce the bias magnetic field B. An electric resistance heater is used to realize a current switch [5] between the two superconducting meandering pickup coils. These are connected to each other with an electrical bypass line. When the heater is activated, by applying $\sim 3\,\mathrm{mA}$ to it, the bypass line becomes normal conducting while the meandering pickup coil remains superconducting.

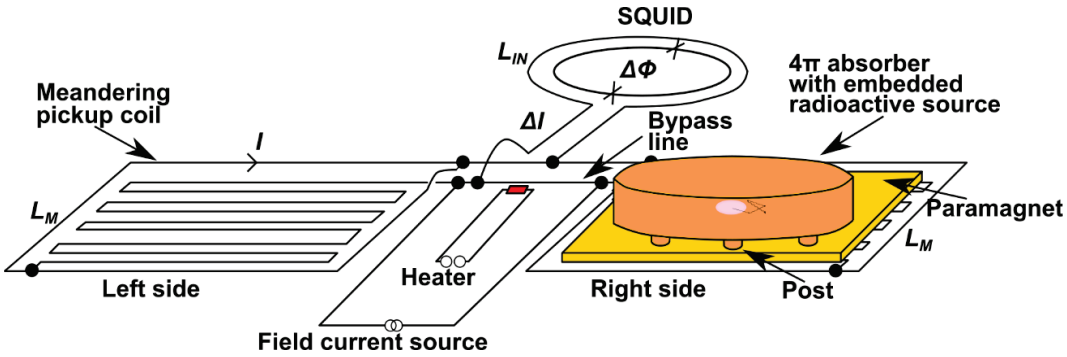

Figure 2. Schematic view of the MMC read out by a SQUID. To show the underlying meandering pickup coil structure, the paramagnet on the left side is not included in the picture.

A 4π gold absorber is thermally linked to the MMC detector via several gold posts [2]. When a decay occurs in the radionuclide source, the kinetic energy of the emitted beta particle is absorbed completely, causing a small temperature increase in the absorber. The heat is transported via the posts to the paramagnet, which due to the temperature dependence of its magnetic susceptibility, changes its magnetization. The corresponding magnetic flux change of the paramagnet is detected by the superconducting meandering pickup coil, which generates the compensating current ΔI. This is coupled to the input coil of the SQUID sensor. Thus, the energy of the radioactive decay in the absorber is proportional to the compensating current. The rise and fall times of the signal pulses depend on the thermal couplings: absorber <-> MMC sensor and MMC sensor <-> thermal bath, respectively. As there are two sensors with reverse polarity on the MMC chip, it is possible to operate it with two absorbers (either giving rise to positive or negative signal pulses, respectively). The design was made in such a way that the left and right sensors are slightly imbalanced. Hence, the net magnetization due to thermal variations can be measured e.g. during a diagnostic test of the detector characteristics.

2 MMC design and SQUID compatibility

To measure high quality beta spectra, one needs to ideally measure every decay of the source in a considered time frame with a high energy resolution over the entire energy range $[0, E_{\mathrm{max}}]$. Hence, the absorber needs to be large enough to completely stop the beta particles of the radioactive decay. When gold absorbers are used, the following thicknesses can be calculated [6]: $260\,\mu\mathrm{m}$ (^{36}Cl, $E_{\mathrm{max}} = 709.5\,\mathrm{keV}$), $60\,\mu\mathrm{m}$ (^{99}Tc, $E_{\mathrm{max}} = 293.8\,\mathrm{keV}$) and $21\,\mu\mathrm{m}$ (^{14}C, $E_{\mathrm{max}} = 156.5\,\mathrm{keV}$).

2019 JINST 14 P08012

At the same time, the absorbers need to have small dimensions (0.25–9 mm^2) to ensure a low heat capacity while also being manageable for source embedding. Thus, microfabricated MMC detectors designed for corresponding absorber heat capacities to measure beta spectra with endpoint energies E_{max} ranging from a few tens of keV up to ≈ 1 MeV were realized in the MetroBeta project [6, 7], see table 1. The constraints of the design optimization were: 1) the heat capacity of the MMC sensor should be matched to that of the absorber, 2) the inductance of the meandering pickup coil should be twice as large as the inductance of the designated SQUID input coil[1] (i.e. $L_M = 2 \cdot L_{IN}$) and 3) the thermal link between the MMC detector and the on chip heat bath pad should allow a signal decay time of ∼ 1 ms at the desired operating temperature. Optimal design parameters concerning the linewidth/pitch of the pickup coil and the meander area/inductance could thus be determined. All five MMC sizes are fabricated on a common silicon wafer, which puts an additional constraint on the optimization and fabrication. In order to calculate the corresponding energy resolution of each design combination,[2] the following fabrication and setup relevant values were used: an erbium concentration in Ag of 310 ppm, a sensor thickness of 3 µm, an operating base temperature of 20 mK, with an assumed SQUID white noise level of 0.35 $\mu\varphi_0/Hz^{1/2}$ and a SQUID 1/f noise level at 1 Hz of 2.6 $\mu\varphi_0/Hz^{1/2}$.

Table 1. Overview of absorbers, SQUID types and MMC detector parameter values per design.

absorber type	XS	S	M	L	XL
material	Au	Au	Au	Au	Au-Cu bilayer
surface shape	circle	circle	octagon	octagon	octagon
diameter	480 µm	600 µm	725 µm	1655 µm	3065 µm
thickness of single foil	15 µm	40 µm	100 µm	300 µm	200 µm: 150 µm (Au:Cu)
absorber heat capacity	8 pJ/K	28 pJ/K	110 pJ/K	400 pJ/K	1.70 nJ/K
designated SQUID type	X1	X1	X1	XS	S
input inductance	2 nH	2 nH	2 nH	27 nH	65 nH
MMC detector type	XS	S	M	L	XL
MMC sensor heat capacity	7.57 pJ/K	17.9 pJ/K	50.6 pJ/K	308 pJ/K	1.17 nJ/K
single meander inductance	3.4 nH	3.1 nH	8.0 nH	56 nH	196 nH
linewidth of pickup coil	2.5 µm	5 µm	5 µm	5 µm	5 µm
pitch of pickup coil	5 µm	10 µm	10 µm	10 µm	10 µm
meander/sensor area (square shape)	$(249\ \mu m)^2$	$(335\ \mu m)^2$	$(538\ \mu m)^2$	$(1427\ \mu m)^2$	$(2663\ \mu m)^2$
expected flux coupling	3.8%	4.0%	2.6%	0.8%	0.5%
optimum field current	38.2 mA	67.8 mA	75.7 mA	63.3 mA	67.1 mA
expected signal size	23.2 $m\Phi_0$/keV	12.9 $m\Phi_0$/keV	6.41 $m\Phi_0$/keV	2.97 $m\Phi_0$/keV	1.61 $m\Phi_0$/keV
expected energy resolution	5.17 eV	9.46 eV	19.1 eV	37.5 eV	74.4 eV

[1]Since high resolution SQUID sensors [8] were already fabricated and available, the MMC designs were adjusted to these.

[2]For the XL absorber type, a Au-Cu bilayer material was considered which can reduce spectrum distortions, caused by bremsstrahlung effects in the absorber, for radionuclide sources with $E_{max} \geq 500$ keV [9]. Its realization will be addressed in a future work.

2019 JINST 14 P08012

3 Absorber preparation and source embedding

An absorber material needs to have e.g. a high stopping power for beta particles (high atomic number Z), allow for fast thermalization, be available in a highly pure form while chemically stable and easy to machine. For these reasons, noble metals such as gold ($Z = 79$) or silver ($Z = 47$) are suitable absorber materials. The process starts with fabricating the absorbers from foils (5N Au foils). Depending on the thickness d of the foil, laser ($d < 90\,\mu m$) or milling techniques ($d \geq 90\,\mu m$) are used to produce a reproducible array of absorbers. Next, the absorber array is prepared for source embedding by cleaning it with organic solvents, strong acids or bases and distilled water. There are several methods to embed a radionuclide source into 4π absorbers. Ion implantation [10] is a laborious technique which requires dedicated facilities but yields very pure embedded samples. In our work, electrodeposition [6] as well as automatic drop deposition [11] are utilized. Manual drop deposition allows for the dispensing of small volumes in the order of 0.1 µl which corresponds to a dried drop diameter of $\sim 1000\,\mu m$. Thus, the manual method is not appropriate for absorbers with an area smaller than approximately $1.5 \times 1.5\,mm^2$. In the case of a Au absorber this corresponds to using an MMC detector of at least size L. However, for typical radionuclide carrier solutions (e.g. ^{36}Cl in 0.05 mol/l NaOH, 33 mg/l NaCl), state of the art automated micro dispensers are able to deposit single drops with volumes of less than 50 picoliters and a placement accuracy of 20 µm. This corresponds to a dried drop diameter of approximately 70 µm. Several tests were conducted using a commercial micro dispenser (microdrop MD-P-826), which demonstrate high reproducibility for the drop dimensions, placement accuracy and source activity, as depicted in figure 3.

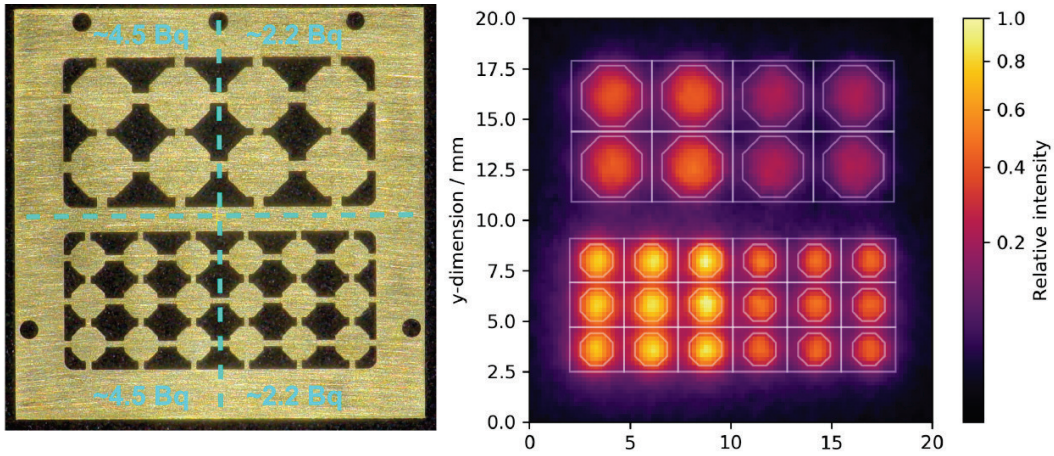

Figure 3. Gold absorber array (left) and an autoradiography plot of the dispensed array (right). The left absorber array half was dispensed with a nominal total activity of 4.5 Bq/absorber and the right absorber array half with 2.2 Bq/absorber.

After depositing the radionuclide on the surface of an array of absorber halves, the array is mounted on an aluminum/glass assembly and a second absorber-half array of the same shape and thickness but without any radioactive source is placed on top of it. Another glass/aluminum plate is put on top of the absorber-source-absorber sandwich and screws of the assembly are fastened to produce a pressure of approximately $1.5\,N/mm^2$. To ensure a leak-proof diffusion welding of the

2019 JINST 14 P08012

gold foils, as depicted in figure 4, the assembly is put into an oven e.g. for approximately 45 min. at 400°C in the case of ^{36}Cl. In general, the appropriate duration and temperature depends on the chemical properties of the carrier solution salts, such as their melting and boiling points. When the assembly has cooled down, the individual absorbers are cut out from the array using a scalpel. The next challenging task is to mount the small absorber onto the MMC detector where it must remain during the overall experiment. This is done in several steps where first, employing a semi-automatic component placement device, droplets of Stycast 1266 are placed between or on the posts of the MMC sensor using a thin wire. The absorber is put on top of the epoxy glue droplets using the placement device, applying a force of approximately 1 N for a few minutes to get an initial adhesion between the two surfaces. However, to ensure a tight thermal connection between absorber and MMC sensor, after the initial adhesion, a larger force of approximately 10 N is applied to the absorber using a custom-built assembly.

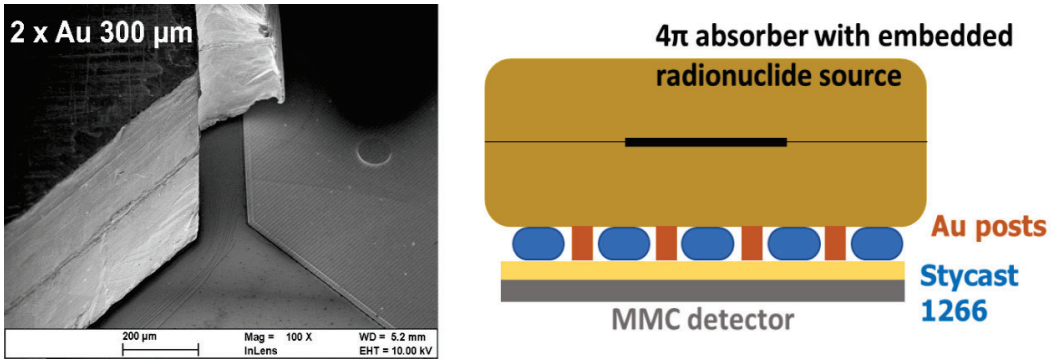

Figure 4. Scanning electron microscope image of a diffusion welded XL absorber (2× Au 300 µm) mounted on an XL MMC detector (left) and schematic picture (right).

4 The beta spectrometer detector module

The newly developed beta spectrometer [6] features a detector module consisting of a gold-plated copper support structure which is operated at temperatures < 20 mK in a commercial dilution refrigerator (BlueFors LD250). The support structure holds the MMC detector and SQUID sensor, as depicted in figure 5. The microfabricated devices are glued to the detector module with GE Varnish or Stycast 1266 and separated with a slit in the support structure to reduce parasitic thermal coupling.

Superconducting NbTi wires and copper wires connect exterior electronics to the Printed Circuit Boards (PCBs) of the MMC detector and SQUID sensor, respectively. While the exterior electronics are at room temperature, sufficient thermalization to the base temperature is realized with Au bonds from the MMC detector and the SQUID sensor to the PCB/gold plated copper support structure. Further electrical connections are realized with superconducting Al bonds (PCB <-> MMC/SQUID and MMC <-> SQUID). Additional features of the detector module are a reference X-ray source, which can be used for energy calibration, and a superconducting magnetic shielding made of aluminum. Due to the vibrations of the dilution refrigerator, the detector module

2019 JINST 14 P08012

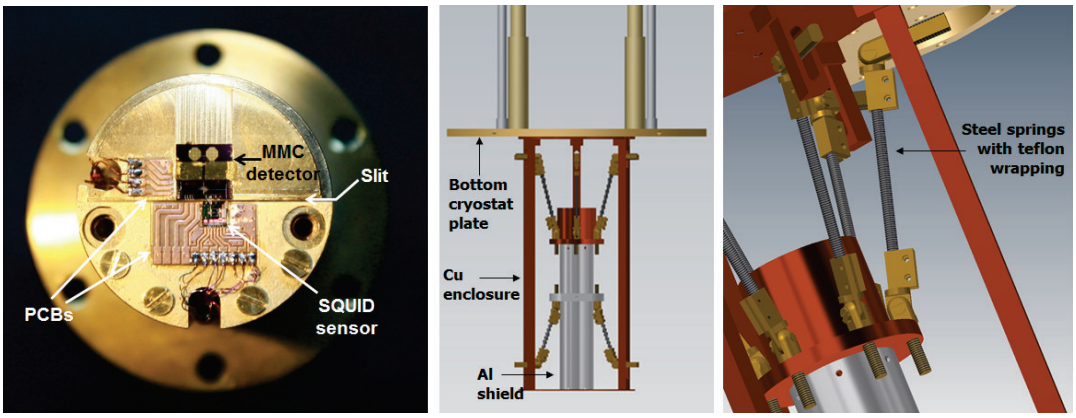

Figure 5. Top view of the support structure (left) and sketches of the detector module mounted in the vibration reducing copper enclosure (right).

is mounted into a copper enclosure and suspended with fabricated steel spirals wrapped in Teflon ribbons. Several thermal straps made of flexible copper braids that connect the bottom cryostat plate with the detector module, ensure the thermalization needed for the measurement.

5 Data acquisition and evaluation

To read out the SQUID current sensor [8], a state-of-the-art commercial SQUID electronics device (Magnicon XXF-1-6/2 + CSE-2) is used. It features a two channel Flux Locked Loop (FLL) that additionally allows us to inject a meander current into the MMC detector of up to 150 mA with a maximum heat switch current of 20 mA. The SQUID FLL output voltage signal is read out using a commercial PCIe digitizer card (Alazar ATS 9462). It comprises two channels which are sampled at 16-bit resolution, each having a maximum sampling rate of 180 MS/s per channel with an input range from ±200 mV to ±16 V. The custom-built measurement routine, which features an automatic reset functionality that enables resuming the measurement when the SQUID electronics lose lock, was developed in LabVIEW. The temperature stability is monitored with a control algorithm in the dilution refrigerator software.

As described above, the output data of the measurements in the setup are signal pulses. In principal, there are two modes of measurement: a) triggered mode i.e. recording pulse windows for all signals that exceed a certain voltage level, which is implemented in the digitizer hardware and b) continuous data acquisition i.e. recording every data point, as depicted in figure 6.

To measure a beta spectrum with high resolution, a histogram of pulse amplitudes with energy calibrated pulses needs to be recorded. The number of required pulses for a 1000 bin spectrum is on the order of $5 \cdot 10^6$. Realistically, the pulses have a 10/90 rise time $\sim$ 10 µs and a 90/10 fall time $\sim$ 10 ms. Assuming an exponential pulse shape and requiring that the pulse height returns to less than 5% of its maximum pulse amplitude, would demand a pulse window of approximately 20 ms (e.g. a pre- and post-trigger of approximately 10 ms). At 4 Bq source activity, one has a pile-up probability (at least one decay occurring during the post-trigger of a previous pulse) of approximately 4% with the conventional assumption of the number of radioactive decays in a time frame being Poisson distributed. The amount of unresolved pile-up, i.e. the probability for at least

2019 JINST 14 P08012

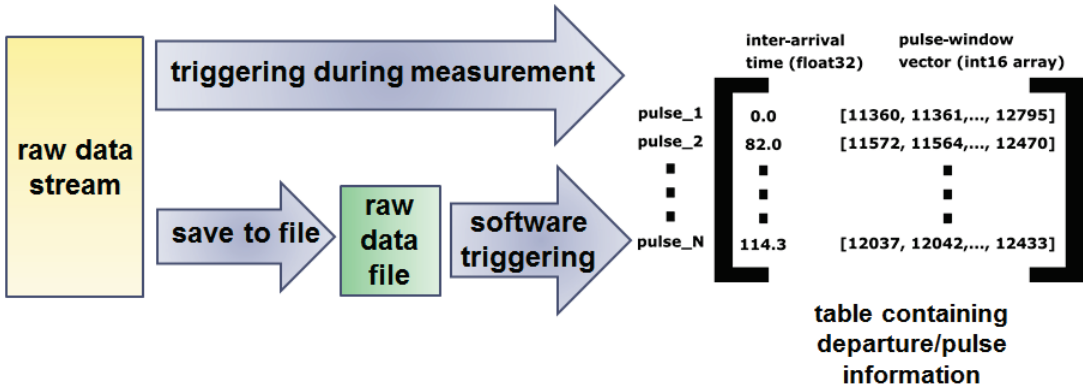

Figure 6. Overview of the measurement and trigger modes.

one decay on the rising flank (1/99 rise time $\sim$ 20 µs) is in the order of 80 ppm. To measure $5 \cdot 10^6$ pulses, the required measurement time is approximately 14 days. Using a sampling rate of 100 kS/s the size of the measurement data sets would be about 20 GB [triggered mode] and 250 GB [continuous data acquisition], respectively.

When using the trigger mode, pulse windows are only recorded around points exceeding the previously set trigger level, i.e. significant departures from the baseline and saved in binary data format files. While a trigger mode measurement is less data intensive and practical for measuring pulses with a high signal to noise ratio (e.g. lines of calibration sources at higher energies), low energy pulses may get lost due to poorly defined trigger levels. Thus, we currently focus on continuous data acquisition with subsequent software triggering.

If the measurement mode is continuous, every data point is saved into a raw data file in binary format. Since the data sets are rather large it is important to have sensible data handling and sorting algorithms, an overview of our approach is depicted in figure 7. The procedures were programmed in Python [12] using compiled code packages such as NumPy, pyTables and pandas to decrease the computation time. Before processing the large data sets, it is sensible to study the noise level in the signal baseline and pulses manually e.g. to estimate the rise and fall times as well as pulse height ranges to set a sensible trigger level and other processing parameters.

When the measurement is finished, the time series of the entire data stream is software triggered to extract the pulse windows. This is achieved by finding departures (peaks/valleys) from the signal baseline. Several kinds of triggers can be used e.g. a slope path trigger which finds consecutive points having a positive/negative slope and when the slope crosses zero, which can be used to get a first estimate of the pulse height. Alternatively, a Constant Threshold Discriminator (CTD) and a Constant Fraction Discriminator (CFD) trigger can be used, see e.g. [13, 14]. When a signal has been found, the peak/valley start index is recorded along with the pulse window i.e. a vector of data points before and after that index. The processing parameters of the algorithm e.g. the slope and window length are set by the user and can be estimated by studying individual pulses before recording the data set (a similar preparation is necessary for the trigger mode option). At 100 kS/s approximately five sample points are recorded for a typical 10/90 rise time of 50 µs and this is sufficient for the software triggering algorithm. The trigger efficiency can be validated by analyzing

2019 JINST 14 P08012

simulated data, with a known number of pulses and realistic noise levels. We plan to address this in a future work.

The processed data is collected in a pulse table in the hdf5 format [15], which is a compact, cross-platform compatible binary data format, that is optimized for efficient data querying (pulse_window_table.hdf5 in figure 7). The pulse table is further evaluated, creating an evaluated pulse table where properties such as pulse-height estimates, inter-arrival times and normalized pulse shapes are calculated (evaluated_pulses_table.hdf5 in figure 7). Now, queries on the evaluated pulse table can be used to select data e.g. for pile-up rejection and pulse-shape classification.

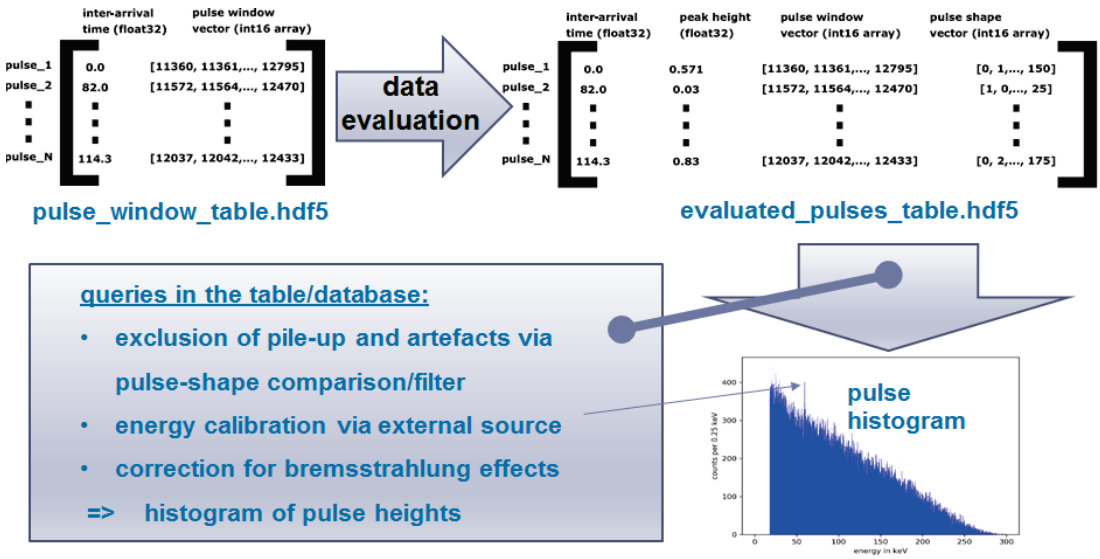

Figure 7. Overview of the data evaluation routines, at the bottom right the pulse histogram of a test measurement of ^{99}Tc is depicted.

6 Test measurement, DAQ evaluation and energy resolution

The program above was carried out for an automatically drop deposited ^{99}Tc radionuclide source (activity ≈ 4 Bq) in a 4π gold L-absorber (thickness $2 \times 90\,\mu$m, 5N Au foil), mounted on an MMC L-detector that was read out by an XS-sized SQUID current sensor. An external ^{241}Am photon source was used for calibration purposes during the measurement. A persistent current of 80 mA was injected into the MMC detector and the acquisition was done in continuous mode at a sampling rate of 200 kS/s for approximately 13 h. The pulse dynamics were as expected (10/90 rise time $\sim 100\,\mu$s, 90/10 fall time ~ 10 ms) and thus there was no significant amount of pile-up since the activity was relatively low. To find the baseline departures, a Butterworth bandpass filter was applied to the raw data and a CFD trigger determined the trigger points of the filtered data. Using a pulse template, based on the average of manually preselected pulses, approximately $1.9 \cdot 10^5$ pulses were extracted from the raw data. The pulse amplitudes were calculated using a standard optimal matched filtering procedure [16–18]. A histogram of the pulse energies is depicted in figure 8, the calibration peak is clearly visible along with typical characteristics of the spectrum. A Full Width at Half Maximum (FWHM) Gaussian fit of the main peak of ^{241}Am indicates that the energy resolution

2019 JINST 14 P08012

is approximately $\Delta E = 590\,\text{eV}$ at 59.54 keV. The energy resolution given in table 1 corresponds to the (idealized) calculated energy resolution of the MMC detector. The degradation of the energy resolution in the test measurement is mainly due to a weaker than expected signal strength caused by several contributing factors: 1) A non-ideal thermalization of the MMC detector. 2) Higher than expected white noise level in the SQUID current sensor. 3) Non-matching heat capacities of the MMC detector and absorber (the relation was 1:1.46 instead of an ideal 1:1). 4) Heat bath temperature variations. The issues 1)–3) can be resolved by refining the corresponding preparation steps and choosing a specific SQUID current sensor of the highest possible quality. The temperature stability can be improved upon by using a more precise thermometer such as a fixed-point device for controlling the base temperature in the dilution refrigerator and placing the heat bath thermometer closer to the detector module. Data correction, that takes the temperature drift into account, could also be implemented in the evaluation software. Furthermore, the electromagnetic interference shielding of the setup can be improved.

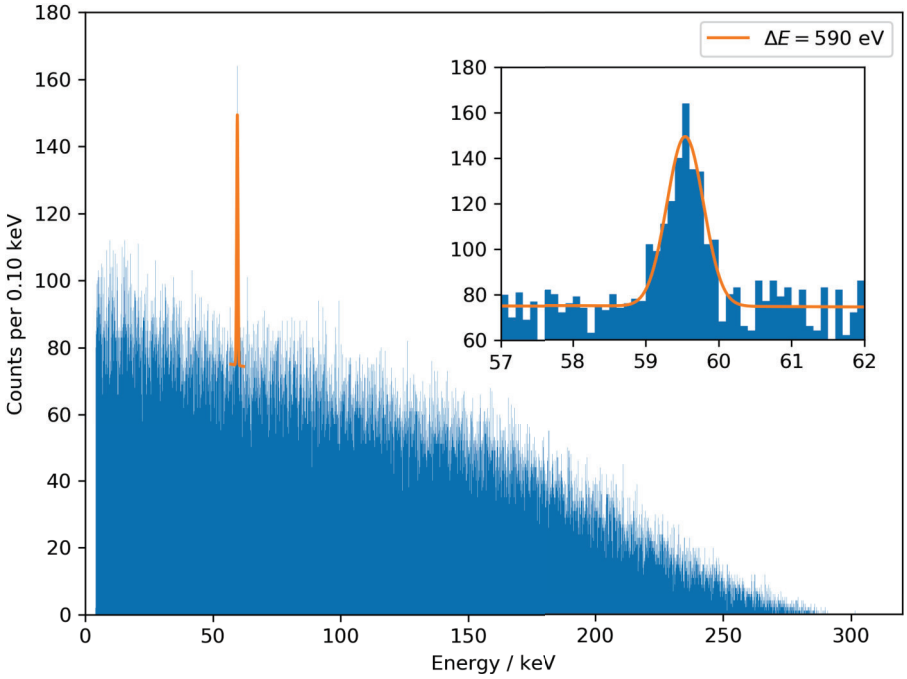

Figure 8. Pulse histogram for a ^{99}Tc ($E_{\text{max}} = 293.8\,\text{keV}$) radionuclide source with an external calibration source (13 h test measurement, sample activity ~ 4 Bq). The calibration peak of ^{241}Am at 59.54 keV is fitted with a Gaussian curve (inset).

7 Conclusion

We have developed a beta spectrometer, including the techniques for absorber and source preparation along with data handling. A test measurement of ^{99}Tc, which involved the interplay of all components, has shown that the setup is capable of high-resolution beta spectrometry with low energy threshold. Several radionuclide measurements of e.g. ^{36}Cl ($E_{\text{max}} = 709.5\,\text{keV}$) and ^{14}C

2019 JINST 14 P08012

(E_{max} = 156.5 keV) using the beta spectrometry setup are in process. For these measurements, calibration sources such as ^{57}Co (14 lines from 0.7 to 706.4 keV) and ^{109}Cd (six lines from 3.2 to 88.0 keV) will be used.

Acknowledgments

This work was supported by the European Metrology Programme for Innovation and Research (EMPIR) grant numbers 15SIB10 MetroBeta [7] and 17FUN02 MetroMMC [19]. The EMPIR initiative is co-funded by the European Union's Horizon 2020 research and innovation program and the EMPIR Participating States. We thank Marco Schmidt and Lars Schikowski at the PTB Berlin for their support in designing and modifying the detector module.

References

[1] A. Fleischmann, C. Enss and G.M. Seidel, *Metallic Magnetic Calorimeters in Cryogenic Particle Detection*, in *Topics in Applied Physics. Vol. 99*, Springer, Berlin Germany (2005), pg. 150.

[2] S. Kempf, A. Fleischmann, L. Gastaldo and C. Enss, *Physics and Applications of Metallic Magnetic Calorimeters*, *J. Low Temp. Phys.* **193** (2018) 365.

[3] A. Fleischmann et al., *Metallic magnetic calorimeters*, *AIP Conf. Proc.* **1185** (2009) 571.

[4] M. Loidl, M. Rodrigues, C. Le-Bret and X. Mougeot, *Beta spectrometry with metallic magnetic calorimeters*, *Appl. Radiat. Isot.* **87** (2014) 302.

[5] H. Rotzinger et al., *Beta Spectrometry with magnetic calorimeters*, *J. Low Temp. Phys.* **151** (2008) 1087.

[6] M. Loidl et al., *MetroBeta: Beta Spectrometry with Metallic Magnetic Calorimeters in the Framework of the European Program of Ionizing Radiation Metrology*, *J. Low Temp. Phys.* **193** (2018) 1251.

[7] MetroBeta Radionuclide beta spectra metrology, available at http://metrobeta-empir.eu/ (2019).

[8] D. Drung et al., *Highly sensitive and easy-to-use SQUID sensors*, *IEEE Trans. Appl. Supercond.* **17** (2007) 699.

[9] M. Loidl, private communication, to be published elsewhere (2018).

[10] F. Schneider et al., *Resonance ionization of holmium for ion implantation in microcalorimeters*, *Nucl. Instrum. Meth.* **B 376** (2016) 388.

[11] R.M. Verkouteren and J.R. Verkouteren, *Inkjet Metrology: High-Accuracy Mass Measurements of Microdroplets Produced by a Drop-on-Demand Dispenser*, *Anal. Chem.* **81** (2009) 8577.

[12] G. van Rossum, *Python tutorial*, Technical Report CS-R9526, Centrum voor Wiskunde en Informatica, Amsterdam The Netherlands (1995).

[13] D. Abbaneo et al., *Design of a constant fraction discriminator for the VFAT3 front-end ASIC of the CMS GEM detector*, 2016 *JINST* **11** C01023.

[14] C. O'Grady, *Stanford Linear Accelerator Center (SLAC): Constant Fraction Discriminator*, https://confluence.slac.stanford.edu/display/PSDM/Constant+Fraction+Discriminator (2019).

[15] The HDF Group, available at http://www.hdfgroup.org (2019).

[16] A.E. Szymkowiak, R.L. Kelley, S.H. Moseley and C.K. Stahle, *Signal processing for microcalorimeters*, *J. Low Temp. Phys.* **93** (1993) 281.

2019 JINST 14 P08012

[17] D. McCammon, *Thermal Equilibrium Calorimeters – An Introduction*, in *Topics in Applied Physics. Vol. 99*, Springer, Berlin Germany (2005), pg. 1.

[18] J.D. Armstrong, *Data Analysis and Double Pulse Detection for the MARE Experiment*, Ph.D. Thesis, University of Miami, Miami U.S.A. (2012).

[19] MetroMMC, *Measurement of fundamental nuclear decay data using metallic magnetic calorimeters*, available at http://empir.npl.co.uk/metrommc/ (2019).

2019 JINST 14 P08012